FBG Thermal Sensing Ring Scheme for Stator Winding Condition Monitoring in PMSMs

Anees Mohammed and Siniša Djurović, *Member, IEEE*

Abstract— This article proposes a random wound stator winding thermal monitoring scheme for permanent-magnet synchronous motors (PMSMs) utilizing an end-winding embedded, ring-shaped, fiber Bragg grating (FBG) thermal sensing array. The scheme enables *in situ* measurement of winding distributed thermal conditions, which is key to their effective health diagnosis and protection. It is designed to provide a thermal sensing point per each individual end-winding coil-end span and thus enable monitoring of the entire winding structure. This was achieved by utilizing FBG thermal sensing multiplexing in a ring-shaped sensor array inserted into the end-winding assembly to ensure desired *in situ* placement of separate sensing elements. The scheme was implemented on an inverter-driven PMSM and its performance examined in tests under healthy and faulted winding conditions. The results demonstrate the capability of effective monitoring of healthy windings distributed thermal status and that of unambiguous identification of localized overheating originating from winding fault, providing monitoring functionality that is largely unattainable by conventional thermal sensing techniques. Finally, the proposed scheme also enables straightforward advanced graphical visualization of the windings' thermal status and, hence, a more effective diagnostic interpretation of thermal data to extract knowledge on locations of increased thermal stress.

Index Terms— Fiber Bragg grating (FBG) technology, localized temperature monitoring, end-winding, permanent-magnet synchronous motor (PMSM), thermal monitoring, winding fault.

NOMENCLATURE

PMSM	Permanent-magnet synchronous motor.
FBG	Fiber Bragg grating.
ITSCF	Interturn short-circuit fault.
2-D TSR	2-D thermal sensing ring.
DE-winding	Drive end winding.
PEEK	Polyetheretherketone.
C_x	Thermal cycles, x is a cycle number.
FS, HS, and LS	Full, half, and low speeds.
FL, HL, and NL	Full, half, and no loads.
xT	Number of shorted turns.

I. INTRODUCTION

DUE to high efficiency and power density and a wide operating range, PMSMs have become the preferred rotating electric machine choice in a number of applications, ranging from modern electric vehicles to military, medical, factory automation, aerospace, and wind energy systems [1], [2], [4], [5]. As PMSMs are often key components in these systems, their integrity and availability are critical [5]. Stator winding is one of the most frequently failed PMSM components [6]. Its failures are invariably related to the insulation system degradation resulting from various operational stresses while in service [7]. Winding faults generally lead to excessive damage and thus motor and system shutdown and extended downtime for maintenance. They are particularly critical in PMSMs due to risk of PM demagnetization by the fault-induced excessive heat and the demagnetizing magnetic field driven by fault current [8].

PMSM winding fault diagnosis has received considerable attention [2], [6], [9]–[12]. The reported diagnostic methods generally rely on noninvasive monitoring and spectral analysis of electrical and/or electromagnetic quantities, as widely explored in induction machines. However, these impose considerable limitations in diagnostic reliability and fidelity in PMSMs due to the challenge in the identification of reliable and consistent fault spectral signatures [6].

Thermal aging caused by overheating is the main contributor to the winding insulation system degradation process and thus winding fault. The insulation system is designed to operate to a permissible temperature limit [7]. There are, however, many practical operating conditions in which stator windings can be uniformly or locally overheated (e.g., running overloading, cycling, unbalanced supply, and partly/fully degraded cooling capability) [13]. Overheating the windings leads to insulation system degradation and eventually insulation breakdown between the adjacent turns, causing the ITSCF is generally considered a winding fault early stage [7]. At this stage, localized overheating in the winding faulted section is generated due to the high current circulating in the shorted turns [13]. Consequently, early-stage winding fault can also constitute a cause of localized overheating, which accelerates the degradation process of the neighboring healthy turns' insulation and thus eventually propagates fault to more advanced stages characterized by increased heat loss [14]. The realization of an effective winding thermal monitoring scheme capable of distributed monitoring of winding thermal conditions, including

uniform and localized overheating, is thus significant for multiple reasons as follows:

1) It could ensure full protection of windings from uniform or localized overheating under normal and abnormal conditions and thus extend insulation lifetime and mitigate winding faults.
2) It could enable advanced fault diagnosis capability by appropriately monitoring developing winding fault-induced localized thermal excitation.
3) It could provide enhanced motor thermal management through improved understanding of proximity to thermal design limits.

The machine winding conventional on-line thermal monitoring techniques are not fully effective in accessing and measuring localized winding thermal hot spots in normal and abnormal conditions. The thermal estimation-based monitoring techniques, such as resistance-based-temperature estimator (model- or injected signal-based), provide only the winding average temperature [15]. The thermal model-based temperature estimator techniques, such as those embedded in modern thermal protection relay microprocessors, are limited by applied model complexity and the challenge in accurately determining its thermal parameters. In addition, prediction of localized heat caused by abnormal conditions using thermal models requires practically inaccessible parameters, such as short-circuit current during winding faults or cooling air speed during deteriorated cooling capability in air-cooled machines [7]. An alternative is provided by the thermal sensing techniques conventionally used in electric machine windings, such as thermocouple or resistance temperature detectors [16]; these, however, impose considerable limitations in a practical application due to the ideally required number of sensing points for winding distributed thermal sensing and the installation complexity caused by sensor size and wiring. In addition, their inherently conductive structure and sensitivity to electromagnetic interference largely limit their embedment in direct contact with winding conductors [13], [15].

An alternative on-line winding hot spot thermal monitoring technique based on the use of coil-embedded FBG sensing technology has recently been reported [17]–[20]. An FBG is a microstructure inscribed in an optical fiber that behaves like a nonconductive and electromagnetically immune sensing element and thus presents an attractive prospect for *in situ* winding sensing applications [17]. An FBG sensor cost is comparable to that of conventional thermal sensors, such as thermocouples and RTDs. The cost of FBG sensing technology application is dominated by the interrogator expense (signal conditioning device); FBG interrogators are largely designed and produced for niche high-value applications and remain relatively costly. However, the attractive multiplexing, electromagnetic immunity, and multiphysical sensing aspects of this technology could facilitate the development of targeted distributed embedded sensing schemes and enable an "all-in-one" sensing system design for advanced monitoring applications. This could significantly reduce the cost of existing monitoring systems through size reduction and provide a high-volume application that could drive the FBG technology

cost down [19]. FBG sensor application in slot sections for on-line stator winding interior thermal monitoring in random wound machines has been reported in the author's recent works [17], [20]. Bazzo *et al.* [17] reported the use of a new *in situ* FBG temperature sensor for healthy random wound stator winding hot spots monitoring, which is fundamental for understanding winding insulation system degradation. Fabian *et al.* [20] reported a proof of concept study of winding fault-induced thermal signature monitoring in induction machines based on the slot-embedded *in situ* FBG sensing configuration.

This article reports a new FBG thermal sensing scheme for healthy and faulty stator winding condition monitoring aimed at enhancing wider acceptance of FBG thermal sensing application in electrical machines by enabling easier implementation and interpretation of this technology. The proposed scheme thus considers key practical application aspects, such as sensing optimization, installation, and measurement interpretation. To this end, a 2-D TSR design embedded in the end-winding section of a random wound stator winding is proposed, which can enable improved awareness of winding thermal status under different operating conditions through facilitating effective monitoring of distributed thermal conditions in its entire structure. The reported 2-D TSR scheme's performance was examined in tests on an inverter-driven PMSM in healthy and faulted winding conditions. The resulting thermal measurements demonstrated the scheme's capability to map the thermal status of the PMSM winding in a wide range of healthy operating conditions. In addition, it is shown that the 2-D TSR is effective in monitoring localized thermal excitation such as arising from winding fault. This allows for recognition and localization of fault events through observation of their thermal signature, as evidenced on the examined PMSM which are known to be challenging for winding fault diagnosis [6]. Finally, effective graphical presentation of 2-D TSR distributed thermal measurements is proposed, which enables a straightforward understanding of the winding thermal status and its operational diagnosis in both healthy and fault conditions.

II. PROPOSED 2-D TSR SENSING SCHEME PRINCIPLES

End windings in random wound stator windings consist of combined coil ends of all stator coils. The coil ends can generally either be uniformly or locally thermally stressed in operation. For clarity, Fig. 1 shows different overheating scenarios in a simplified schematic of a simple three-phase random wound winding configuration containing two coils per phase (green, orange, and black coils).

Uniform overheating can be caused by operating conditions, such as transient or running overloads, fully reduced cooling capability and a high ambient temperature. In such conditions, all coil ends are uniformly overheated, as indicated by the blue dashed rectangle in Fig. 1. From thermal protection and monitoring perspective, a single thermal sensor attached to the end-winding structure at any point could ensure effective monitoring and detection of this condition.

Localized overheating can be caused by conditions, such as unbalanced phase currents, partially deteriorated
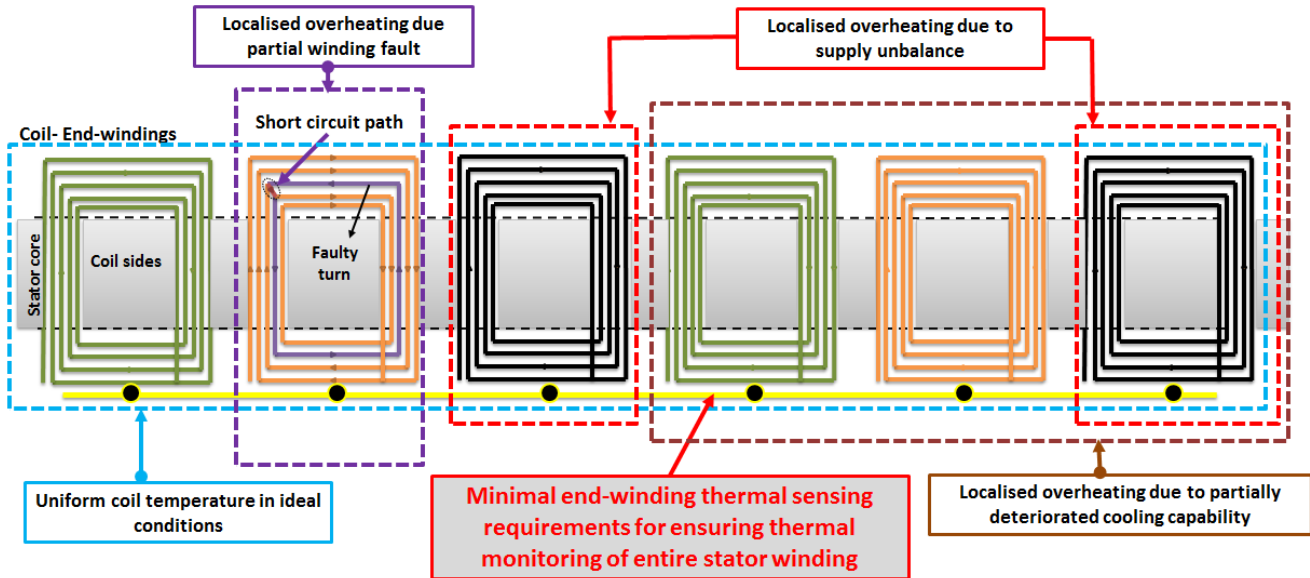
Fig. 1. Simple schematic of three-phase stator winding highlighting different overheating scenarios.

cooling capability, and early winding fault. Unbalanced three-phase winding currents result in uneven individual phase temperatures, where one phase winding can be hotter than others, as shown in Fig. 1 by the red dashed rectangle on the coils shown in black. To monitor the unbalanced current-induced localized overheating, a single thermal sensing point per phase in the end winding would be required. A partially deteriorated cooling system can cause a partial reduction in the heat dissipation capability from stator coils to ambient, resulting in overheating of the coils whose heat dissipation pathway is affected by the cooling deterioration; this is shown in Fig. 1 by the brown dashed rectangle showing an assumed overheated winding section due to deteriorated cooling capability [21]. Under this condition, at least one sensing point per affected area would be required to ensure registering of localized heat. Early stages of short-circuit fault can also cause localized heat in the faulted turns, shown in Fig. 1 by the purple dashed rectangle highlighting an assumed faulted coil. From a thermal monitoring point of view, one sensing point for each stator coil end would be needed to ensure the measurement of thermal excitation resulting from an arbitrary ITSCF.

The sensing requirement analysis for different overheating scenarios suggests that a single thermal sensing element per every individual coil-end span in the end-winding structure is sufficient to ensure thermal monitoring of the entire stator winding, as shown in Fig. 1. The end winding is conventionally instrumented with a number of thermal sensing elements (generally three sensing elements, one per phase) [22], [23]. However, only three thermal sensing points in the end winding can readily miss localized overheating and are not fully sufficient to provide effective monitoring of the entire stator winding, as demonstrated by a large number of operating machines that, in addition to any existing dedicated protection system, despite being instrumented in this manner have failed in-service as a result of insulation breakdown [23], [1]. In general, the short-circuit fault thermal condition is the most critical in terms of winding overheating. This is

due to the fact that the level of fault-induced heat can be excessive and has a rapid rate of change, and its location in the winding structure is unpredictable. A thermal monitoring technique capable of registering winding fault-induced localized heat can consequently be expected to be capable of monitoring other possible winding overheating conditions. This article, therefore, examines and evaluates the proposed thermal sensing scheme under ITSCF conditions.

III. EXPERIMENTAL APPARATUS DESCRIPTION

The proposed 2-D TSR application for stator winding thermal monitoring under healthy and faulty conditions was experimentally investigated in tests on a commercial PMSM. The 2-D TSR was designed and prototyped to conform to the examined PMSM stator winding configuration. This section describes the used experimental apparatus, including the test PMSM, its winding configuration modified for fault emulation, the 2-D TSR design and embedment, and the test rig system setup.

A. Examined PMSM Design

The examined machine is a 5.5-kW three-phase, 400-V, six-pole, totally enclosed fan-cooled (TEFC) PMSM by Lafert. Its nameplate specifications are shown in Table I and its stator winding configuration in Fig. 2. The stator winding is of concentric and stranded design; each phase contains six-series-connected coils, where each coil is wound with six parallel strands of 23.5 AWG enameled copper wire. Since the test motor is a TEFC design, its stator winding highest temperature points are expected to be located in the DE-winding; the sensing points of interest in this article are therefore located in the DE-winding structure. Fig. 3 shows the coil-ends' arrangement in the test machine DE-winding. The coil ends are distributed in three layers (one layer per phase): phase C coil ends are in the bottom layer close to the frame bore surface, the midlayer coil ends belong to phase B, while the

TABLE I
PMSM MOTOR SPECIFICATION

| PMSM Data	Type: HPS1141500
Rated Power / Voltage / Current	5.5 kW / 400 V / 11.5A
Frequency / Rated speed	75 Hz / 1500 rpm
Torque	35 Nm
Back EMF	301V
Ke / Kt	1.92 / 3.1
Resistance / inductance	1.18 Ω / 12.9 mH
Pole number/ Rotor configuration	6 / Surface mounted magnet
Slot number stator	39
Insulation class / Temperature rise class	F / B
Duty cycle type rating	S1
Cooling design	IC 411
Design standard	IEC 60034
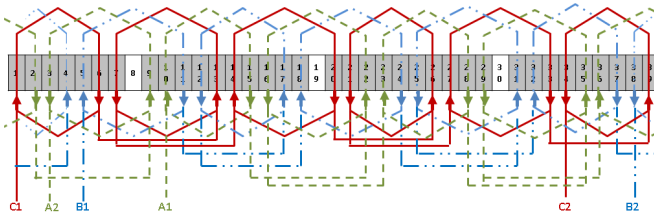
Fig. 2.   PMSM stator winding configuration.
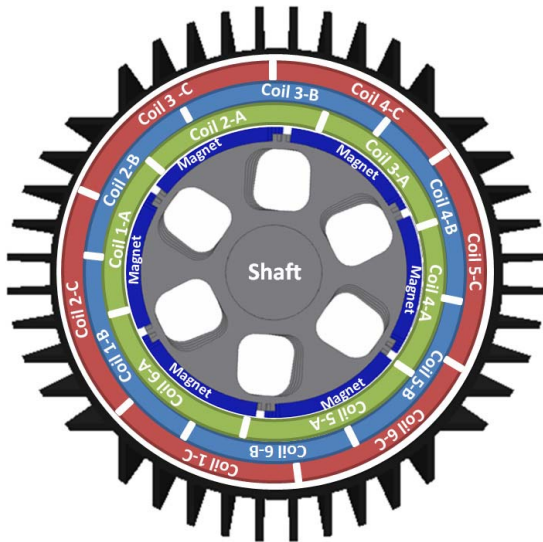
Fig. 3.   Three-phase coil-ends' arrangement in the DE-winding.

top layer facing the air gap is phase A coil ends; the layers are insulated from each other by phase insulation.

B. 2-D TSR Design and Installation

Based on the coil-ends' arrangement in the targeted DE-winding shown in Fig. 3 and the proposed optimized sensing requirements of having one thermal sensing point per each individual coil-end span, two FBG thermal sensing arrays, A and B, were designed and developed, as shown in Fig. 4(a). The individual array FBG heads were spaced to enable sensing point positioning in target DE-winding structure locations, as shown in Fig. 4(b) and (d). The two arrays form the 2-D TSR; each contains six thermal sensing points (FBG heads) imprinted in a bend-insensitive single-mode polyamide fiber. The length of each FBG head in the two arrays is 5 mm and their central Bragg wavelengths are distributed within the light bandwidth of 1530–1560 nm, with the average reflected Bragg bandwidth of ≈0.3 nm and the reflectivity of ≈80%. The measured average FBG temperature sensitivity is ≈12 pm/°C. To protect the sensing fibers and eliminate mechanical excitation of FBG heads and, hence, any associated FBG inherent thermomechanical sensitivity caused measurement error, the FBG arrays were packaged in PEEK capillaries [17]. PEEK has unique features that make it a fitting choice for this application; it is electrically nonconductive and has high mechanical strength accompanied with high flexibility, and its melting point temperature is ≈350 °C that is considerably greater than maximum temperatures expected in conventional electric machinery. PEEK's high mechanical strength ensures FBG sensor integrity, while its flexibility enables distributed temperature monitoring by facilitating effective array sensor package routing that conforms to end-winding geometry. The proposed design combines the FBG multiplexing feature with the flexibility of PEEK to deliver a versatile 2-D TSR array sensor for the examined application. However, the general FBG array-based thermal sensing ring principles put forward in this article can be readily adapted to enable the application and development of more effective distributed thermal sensing scheme in a wide range of random wound end-winding structures.

Array-A was embedded between the coil ends of phases A and B and array-B between phase B and phase C coils ends. The FBG heads' positions are coded as shown in Fig. 4(b) and (d), starting from the bottom of DE-winding in the clockwise direction (array-A sensing heads with odd numbers and those belonging to array-B with even numbers). This provides an optimized 2-D TSR design having sensing locations (i.e., FBG heads) circumferentially distributed with an ≈30° separation between the adjacent points; this layout ensures at least one sensing point for each coil-end span (for example, FBG 1 monitors coil5-A and coil6-B and FBG2 monitors coil1-C and coil6-B). To enable FBG sensors installation and winding fault emulation, the stator was rewound. The 2-D TSR embedment in the DE-winding was achieved as follows. Once the winding coils were fully inserted in stator slots and secured by the slot top insulation liner and wedges, the PEEK capillaries were embedded between the targeted coil-ends. the end windings were then tied and the winding impregnated. Finally, the FBG arrays were inserted in appropriate PEEK capillaries. For the FBG installation in the winding slot section, the procedure described in the authors' previous work was followed [20].

C. Winding Modification for Fault Emulation

To evaluate the proposed 2-D TSR capability to monitor localized thermal excitation, such as arising at outset of ITSCFs, and hence fault diagnosis capability, the windings
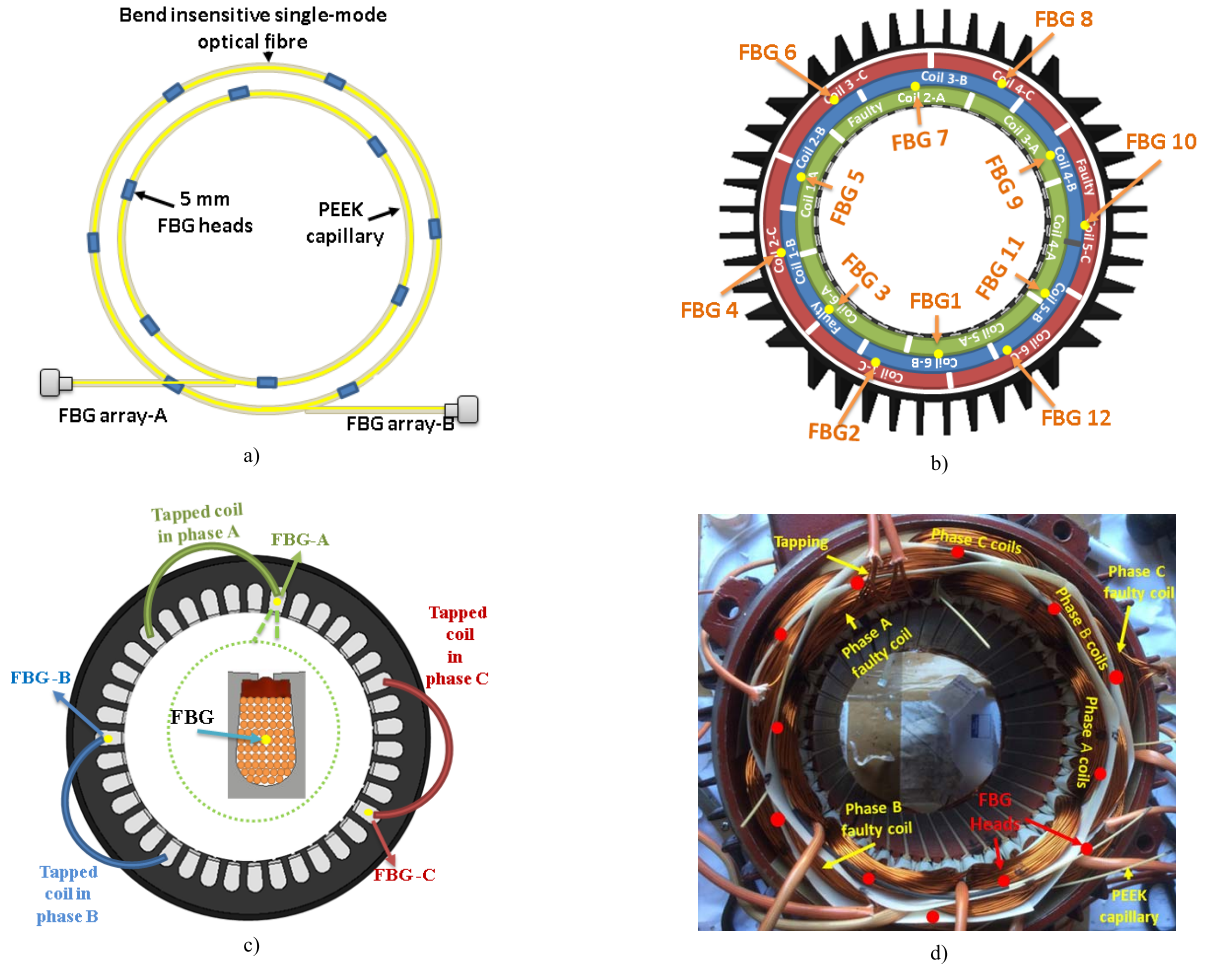
Fig. 4.　2-D TSR design and location in the examined PMSM windings. (a) 2-D TSR: formed by two FBG arrays that consist of six 5-mm FBG heads. b) 2-D TSR sensing point (FBGs) distribution within the PMSM end winding. (c) Tapped coils' position in PMSM winding for fault emulation. (d) Photograph of the DE-winding embedded with FBG sensor positions.

TABLE II
PMSM WINDING FAULT EMULATION

Phase	Faulty coil	Location in DE-winding	shorted turns number (ST)		
			2 shorted turns	5 shorted turns	10 shorted turns
Phase A	coil2-A	top (see Fig.4.C)	2TA	5TA	10TA
Phase B	coil1-B	right (see Fig.4.C)	2TB	5TB	10TB
Phase C	coil5-C	left (see Fig.4.C)	2TC	5TC	10TC

were modified during rewinding to include tappings in specific coils for fault emulation. ITSCFs emulation in three different coils was enabled, one in each phase. Table II shows the details of the faulted coils, their physical locations, and the examined shorted turns number for each fault case conditions. The examined PMSM is designed with a stranded winding configuration; each of the six-series-connected coils forming a phase winding contains 138 turns and is made up of six parallel strands having 23 turns each, as shown in Fig. 5 for phase B winding. For fault emulation purpose, one strand in the targeted coil per phase was modified with tappings to enable emulation of ITSCF scenarios involving different shorted turns numbers (2, 5, or 10) providing different fault severity levels, as shown in Table II. For illustration, Fig. 5 shows the tapped turns in coil1 of phase B. Identical tappings were applied to

phases A and C in the targeted coils. Fig. 4(c) and (d) shows the tapped coils' locations.

D. Laboratory Test System

A test rig was built to enable operating the PMSM under healthy and faulty conditions and facilitate on-line thermal monitoring performance assessment of the installed FBG 2-D TSR. The rig layout is shown in Fig. 6. The test PMSM instrumented with the 2-D TSR system was operated in closed-loop vector control using a 7.5-kW (Parker 890SSD) drive, which was automated via DSE Lite software package. To enable operation in loaded conditions, the PMSM was coupled to a dc machine controlled by a Parker 590SSD dc drive. The *in situ* FBG 2-D TSR and slot sensors were interrogated by a commercial interrogator unit (SmartScan)
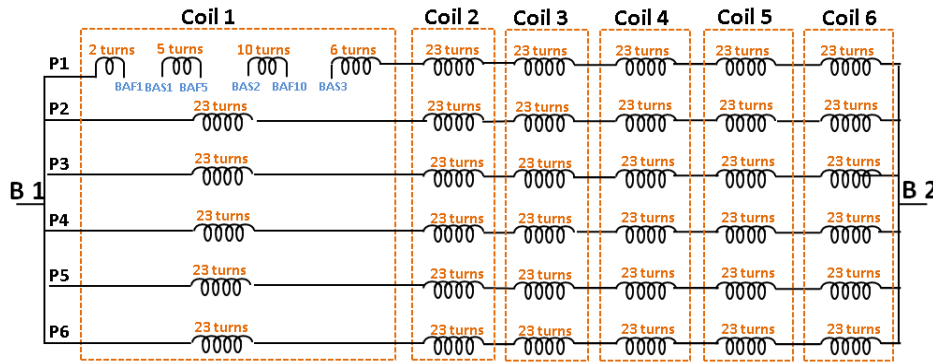
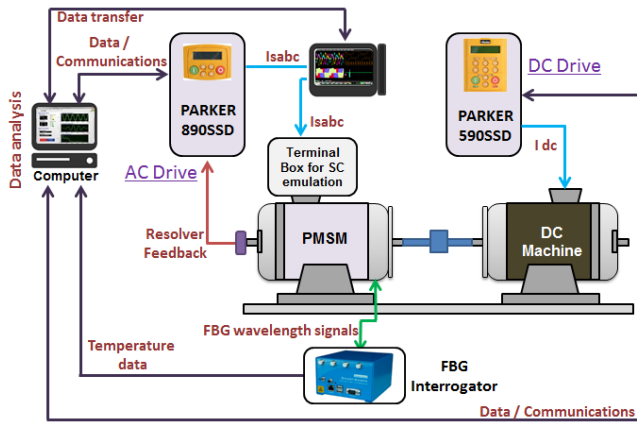Fig. 5.   Modified phase B winding configuration.

Fig. 6.   Test-rig setup.

at a sampling rate of 10 Hz. LeCroy CP150 current and ADP300 voltage probes operated by a LeCroy 434 digital oscilloscope were used for on-line measurement of relevant currents and voltages, including those in the faulted coil.

IV. EXPERIMENTAL RESULTS AND DISCUSSION

Experimental tests were conducted to evaluate the performance of the proposed *in situ* 2-D TSR design for healthy winding thermal condition monitoring and examine its capability to enable detection and diagnosis of early-stage winding fault. The examination was conducted under a range of different thermal conditions applied to the PMSM during healthy and faulty conditions. This was practically achieved by applying a series of IEC 60034-1 standard defined S1 duty cycles on the test motor at different speed and load levels. The S1 duty cycle is defined as "operation at a constant load maintained for a sufficient time to allow the machine to reach thermal equilibrium" [22]. Table III shows the examined S1 duty cycles. Nine different S1 duty cycles were examined in total; their respective load and speed levels are shown in Table III.

A. Healthy Winding Condition Monitoring Evaluation

This section presents and discusses the obtained on-line 2-D TSR thermal measurements under healthy condition. It aims to evaluate the 2-D TSR performance and understand

TABLE III
APPLIED S1 DUTY CYCLES TO THE EXAMINED PMSM

Examined cycles	Cycle speed	Cycle load	Cycly stator	Phase resistance @ winding	Cycle abbreviation
1	1500 rpm (100 % rated speed (FS))	100 % load (FL)	≈ 11 A	1.45Ω @ 80°C	C1: FS-FL
2		50 % load (HL)	≈ 5.5 A	1.33Ω @ 53°C	C2: FS-HL
3		0 % load (NL)	≈ 0.9 A	1.28Ω @ 43°C	C3: FS-NL
4	750 rpm (50 % rated speed (HS))	100 % load (FL)	≈ 11 A	1.49Ω @ 89°C	C4: HS-FL
5		50 % load (HL)	≈ 5.5 A	1.32Ω @ 51°C	C5: HS-HL
6		0 % load (NL)	≈ 0.9 A	1.25Ω @ 35°C	C6: HS-NL
7	375 rpm (25 % rated speed(LS))	100 % load (FL)	≈ 11 A	1.55Ω @ 101°C	C7: LS-FL
8		50 % load (HL)	≈ 5.5 A	1.31Ω @ 49°C	C8: LS-HL
9		0 % load (NL)	≈ 0.9 A	1.23Ω @ 31°C	C9: LS-NL

the examined PMSM winding thermal status under healthy condition.

1) Evaluation of 2-D TSR Performance and Winding Thermal Status Under Different Load Conditions: In this test, three S1 duty cycles (C1–C3 in Table III) were separately applied to the PMSM. Fig. 7 shows the steady-state thermal measurements obtained by the 2-D TSR for the three applied S1 duty cycles; the measured ambient temperature during testing was ≈21 °C. The 2-D TSR thermal measurements are presented in a spatially distributed thermal web form that enables enhanced physical interpretation of the obtained localized thermal conditions and their straightforward correlation to the actual winding/machine geometry. The web radial lines represent the reference directions of the thermal sensing points (i.e., FBG heads' locations in DE-winding) with respect to the reference point in the cross-sectional center of the machine geometry [see Fig. 4(b)]. The web concentric circles represent constant temperature gradients shown for illustration purposes in 10 °C steps.

The blue, green, and red quasi-circular patterns plotted in the thermal web in Fig. 7 are the temperatures measured by the 2-D TSR's 12 FBG heads in NL (C3), HL (C2), and FL (C1) conditions, respectively. Individual dots in the plotted thermal patterns correspond to the actual steady-state measured temperatures by the corresponding individual 2-D TSR FBG heads. The presented distributed thermal measurements are manifested in an almost uniform circular shape, thus illustrating, as expected, the nearly even distribution of the radial temperature levels measured in the examined motor windings in healthy conditions; a temperature difference between 2-D TSR FBG heads of up to ≈3.5 °C was measured at steady state. It can also be observed that the measured
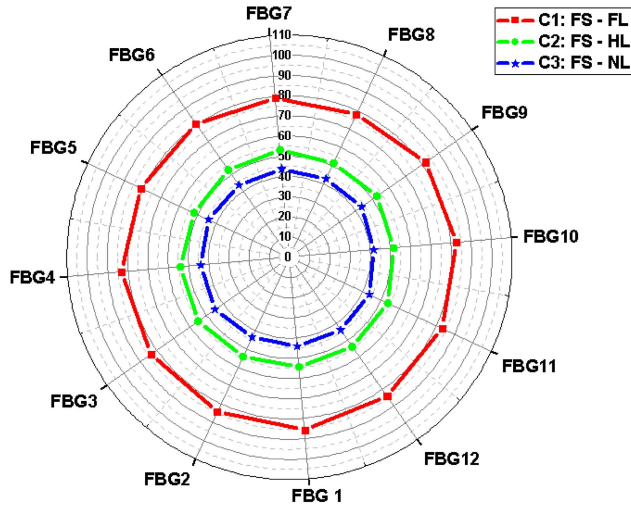
Fig. 7. Thermal web measurements at rated speed and different load conditions.
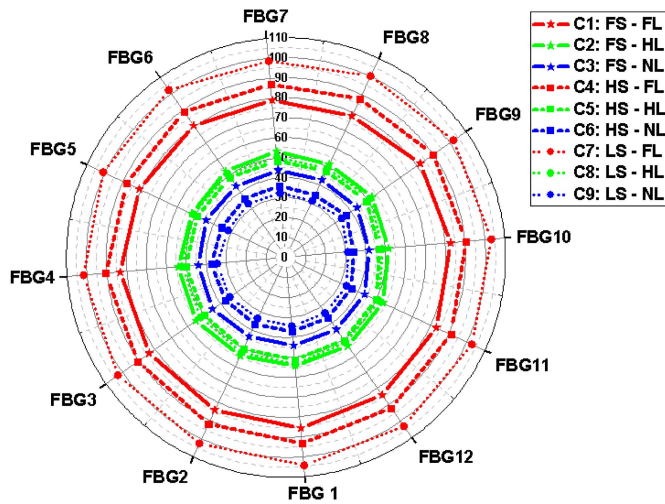

Fig. 8. Thermal web measurements at different speed/load conditions.

thermal patterns' radius increases with load, reflecting the rise in the monitored end-winding internal thermal hot spots due to loss increase with load; for the examined PMSM, this is seen to increase from an average of ≈42 °C at NL to ≈53 °C at HL and ≈80 °C at FL (temperatures obtained by averaging the respective radii of the corresponding thermal patterns).

2) Evaluation of 2-D-TSR Performance and Winding Thermal Status Under Different Speed Conditions: In this test, the PMSM was exposed to a series of S1 duty cycles (C1–C9) at three different speed levels and each speed level was applied at different load levels. The test motor is a totally enclosed rotor fan-cooled design where cooling capability is operating speed dependent. The winding internal thermal status is thus expected to vary considerably with speed variation. This change is generally expected to be further enhanced by the fact that some of machine loss components, such as core and mechanical losses, are also speed dependent.

Fig. 8 shows the obtained thermal webs for all examined S1 duty cycles. The presented thermal measurements demonstrate the variation in the winding internal temperature due

to variation in the PMSM speed and thus the variation in speed-dependent loss components' magnitude and cooling capability. The degradation in the cooling capability and thus winding heat dissipation with reduction of operating speed is most apparent when FL condition is considered (C1, C4, and C7). The average radius of the FL thermal web patterns (red) is seen to increase from ≈80 °C at FS-FL (C1) to ≈89 °C at HS-FL (C4) and further to ≈101 °C at LS-FL (C7). The expected general reduction in loss components, such as core iron loss and mechanical loss with speed, is seen to be insufficient to compensate for the reduction in cooling capability and maintain the winding temperature at a constant level. In contrast, the radii of the thermal patterns at HL (green) show a slight decrease of ≈4 °C with speed reduction from FS-HL (C2) to LS-HL (C8), illustrating that the winding internal temperature decreases with speed reduction at HL conditions. This decrease is further magnified at NL, where the average temperature reduces from ≈43 °C at FS-NL (C3) to ≈31 °C at LS-NL (C9). This thermal behavior can be explained by the decrease in loss components (iron and friction) with speed reduction that can offset the speed reduction caused decrease in winding heat dissipation to the ambient; the rate of heat generated within the test motor to heat dissipated is maintained at an almost constant level at HL and decreased at NL.

The thermal measurements obtained and presented in this section illustrate the efficacy of the proposed 2-D TSR to monitor and map the stator winding thermal dynamics under different operating conditions.

B. Localized Thermal Excitation Monitoring for ITSCF Diagnosis

This section examines the 2-D TSR application for early ITSCF diagnosis in experiments involving various faulty operating conditions. The ITSCF-induced thermal signature was monitored and analyzed for different fault severity and location.

1) Fault Test Procedure: The test procedure applied for each experimentally examined fault condition involved waiting for the thermal equilibrium to first be achieved for healthy machine operating at the examined thermal cycle; a short-circuit fault then is induced and maintained for a 60-s period. To practically emulate short-circuit fault conditions without permanently damaging test machine windings, the circulating current in the shorted turns was limited at a maximum of 15 A at rated conditions (≈130 % of rated current) using an external resistance connected in series with the short-circuit path. The short-circuit current limit was set based on undertaking offline dc thermal excitation tests.

2) ITSCF Thermal Signature Monitoring: To practically examine the 2-D TSR capability to detect ITSCF-induced localized heat loss (i.e., fault thermal signature), ITSCFs were induced in phase A-coil2 with shorted turns cases (2TA, 5TA, and 10TA; see Table II) at rated conditions (C1), following the procedure described in Section V-B1. Fig. 9 shows the obtained measurements at the end of the fault period. Fig. 9(a) shows the 2-D TSR reported thermal pattern in healthy conditions, seen to be manifested as an
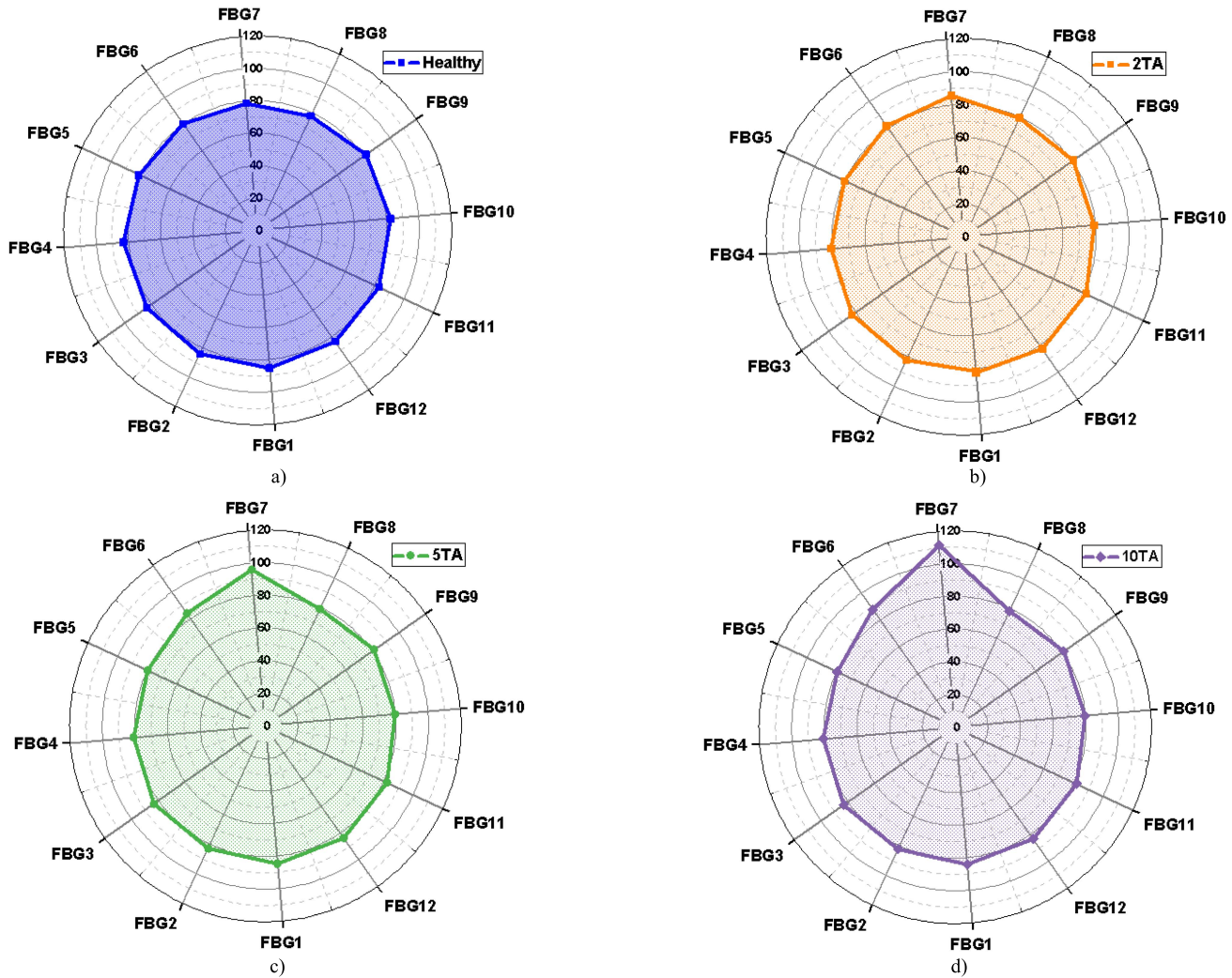
Fig. 9.   2-D TSR-induced thermal patterns for ITSCF diagnosis measured in rated conditions (C1). (a) 2-D TSR thermal pattern in healthy conditions. (b) 2-D TSR thermal pattern for a two shorted turn fault in phase A. (c) 2-D TSR thermal pattern for a five shorted turn fault in phase A. (d) 2-D TSR thermal pattern for a ten shorted turn fault in phase A.

almost uniform quasi-circular shape with an average radius of ≈79 °C, as discussed in Section IV-A. However, with ITSCF presence, the observed quasi-circular thermal pattern alters, reporting temperature-level increase in the direction of FBG6 and FBG7. This trend is magnified with fault severity increase, as seen in the measurements shown in Fig. 9(b)–(d) for two, five, and ten shorted turns cases, respectively. The 2-D TSR FBG6 and FBG7 were capable of register-ing the ITSCF-induced heat in coil2-A since these FBG heads are located close to the faulty coil [see Fig. 4(b)]. However, FBG7 recorded a relatively higher temperature when compared to FBG6; this is because in this fault case, FBG7 is the sensing head in direct contact with the faulted coil. FBG7 measures the temperatures of ≈85 °C, ≈96.8 °C, and ≈112.2 °C in two, five, and ten shorted turns tests, which corresponds to ≈6 °C, ≈17.8 °C, and ≈33.2 °C temperature rise above the healthy winding operating temperature of ≈79 °C at the examined condition. The presented experimental data demonstrate the ability of the proposed 2-D TSR design for ITSCF detection and fault severity diagnosis. The 2-D TSR observed thermal

patterns also show the capability of fault location identification within the winding structure, which is further investigated in Section V-B2.

3) Thermal Signature Monitoring for Fault Location Diagnosis: This section examines the 2-D TSR potential to enable advanced diagnostic capability, focusing on fault location diagnosis. To this end, a number of ITSCFs were induced in different locations within the examined PMSM winding structure. Faults were separately induced in phases A–C and in locations discussed in Section III-C; see Table II at all examined fault severities and at rated operating conditions (C1). Fig. 10 shows the measured thermal patterns for all examined fault cases.

Three distinct thermal-level increase regions can be observed in experimental data; each of these indicates esca-lation of localized thermal excitation in the windings, cor-responding to ITSCF-induced heat locations as defined by the three emulated fault positions. When the fault is induced in coil1-B, the thermal-level increase region appears on the left side of the corresponding thermal web, where FBG3 and
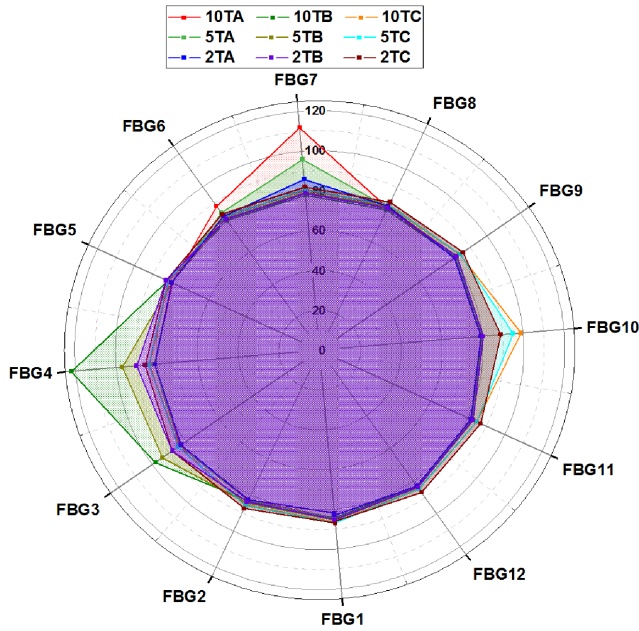
Fig. 10.   Thermal web measurements for different fault location and severity.

FBG 4 are located; FBG3 and FBG 4 are the sensing heads nearest to the faulty coil [see Fig. 4(b)]. When the fault is introduced in Coil5-C and Coil2-A, the thermal -level increase regions are seen to displace to the right and top of the reported thermal web, respectively. The observed thermal increase regions show temperature gradients that clearly correspond to the increase in the examined shorted turns number.

The measured thermal patterns in Fig. 10 show the 2-D TSR design's ability to facilitate effective identification of fault physical location within the winding structure. In addition, the results demonstrate the schemes' capability to also identify the faulty coil and thus the faulty phase. This can be illustrated by considering, for example, the measurements obtained for the coil2-A fault case along with the arrangement of the coil ends and FBG heads in the end-winding area close to the fault location [see Fig. 4(b)]. The coil ends located in this section of the end winding belong to coil2-A, coil3-B, coil3-C, and coil4-C and are monitored by FBG6, FBG7, and FBG8. In case fault occurs in one of the abovementioned coils, the temperature rise levels measured simultaneously by the three colocated FBG heads can enable identification of the faulty coil and phase; when fault occurs in coil2-A, FBG7 is expected to show higher temperature rise than FBG6 and FBG8, which is clearly reported in the corresponding measurements shown in Fig 10.

Similarly, if a fault occurs in coil3-B, FBG7 and FBG8 are expected to show higher temperature rise and when fault occurs in coil3-C or coil4-C FBG6 and FBG8 are expected to show higher temperature rise, respectively. The same principles can be applied to faults in other end-winding sections in order to enable location diagnosis.

The measurements in Fig. 10 indicated that the 2-D TSR measured fault thermal signature magnitudes are different for identical fault severity present at different locations. For example, FBG4 measures a temperature of ≈122 °C for

a ten shorted turns fault induced in coil1-B (10TB), whereas FBG7 and FBG10 measure ≈111.8 °C and ≈98 °C for the same fault level emulated in coil2-A (10TA) and coil5-C (10TC), respectively. This can be explained by the nature of the phase coil-ends' arrangement in the test motor end winding (see Fig. 3) and the nature of radial heat dissipation in the test motor design; phase B coil ends are located between phases A and C coil ends and individual phases are mutually separated by phase insulation. This arrangement reduces the dissipation rate of the fault-induced heat from phase B at the outset of ITSCF. Thus, in case of ITSCF in phase B, 2-D TSR registered the highest temperature level for all examined fault severities, which was measured by FBG4. When ITSCF was induced in phase C the 2-D TSR registered the lowest temperature rise levels, measured by FBG10. This is because phase C is located close to the frame bore surface allowing faster dissipation of fault-induced heat. In the case of ITSCF induced in phase A, the measured temperature rise levels were lower than those observed for fault in phase B and higher than those measured for phase C fault, since phase A coil-ends' location (at the air gap) imposes slower heat dissipation than in case of Phase C fault but still provides a degree of cooling due to airflow in the air gap. It can be concluded that fault in phase-B can be considered the most critical ITSCF location in the examined motor winding in terms of the resulting thermal stress and, thus, the fault magnitude and speed of development. Finally, the noticeable difference between FBG3 and FBG4 readings can be explained due to the fault location within the coil 1-B conductors being located nearer to the coil side adjacent to coil 2-C, thus generating higher thermal excitation in the FBG4 sensor position.

### C. Fault Thermal Signature Analysis Under Different Load/Speed Conditions

Section V-B examined the sensing performance of the proposed *in situ* 2-D TSR for ITSCF diagnosis, including fault-induced localized overheating detection and fault severity and location diagnosis. However, this assessment was conducted only at rated operating conditions (C1: FS and FL). However, modern electric machines are largely inverter driven to operate in variable speed and load conditions. Therefore, this section examines the 2-D TSR diagnostic performance and the fault thermal signature behavior under a wider range of load and speed conditions. The presented analysis also enables the identification of the examined PMSM critical operating points in ITSCF conditions.

1) Different Load Conditions: All ITSCF cases examined in Section IV-B3 under FL condition (C1) were examined here for operation in NL and HL conditions (C2 and C3) to enable observation of the fault-induced thermal signature and sensor performance with load variation only.

For illustration, Fig. 11 shows the obtained thermal measurements for the examined ITSCFs with two, five, and ten shorted turns in coil5-C under NL (C3), HL (C2), and FL (C1), respectively. The presented thermal measurements are obtained by FBG10, which is the FBG head monitoring coil5-C. Fig. 11(a) shows the measured temperature rise
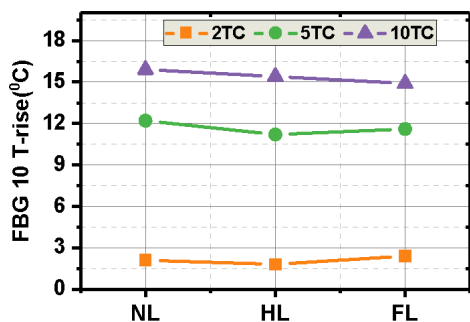
(a) Measured T-rise by FBG10 for 2, 5 and 10 shorted turn fault in phase C
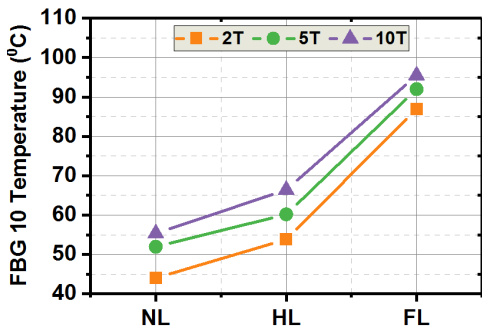
(b)Measured Temperature by FBG10 for 2, 5 and 10 shorted turn in phase C

Fig. 11. Fault-induced thermal signature behavior at different load levels. (a) Measured T-rise by FBG10 for two, five, and ten shorted turn fault in phase C. (b) Measured temperature by FBG10 for two, five, and ten shorted turn in phase C.

(a) Measured T-rise by FBG10 at FL for the examined speeds

(b) Measured temperature by FBG10 at FL for the examined speeds

Fig. 12. Fault-induced thermal signature behavior at different speeds. (a) Measured T-rise by FBG10 at FL for the examined speeds. (b) Measured temperature by FBG10 at FL for the examined speeds.

(healthy to faulty) and Fig. 11(b) shows the actual measured temperature for each examined fault case. The data in Fig. 11(a) indicate that load variation does not result in a considerable variation in the fault-induced heat and thus its thermal signature for a given constant fault level; the measured temperature rise-level difference remains within ≈2 °C. However, it can be noted that there is a slight decrease in the fault-induced thermal signature with load increase at high fault severity levels (five and ten shorted turns). This is because of the shorted turn's resistance temperature dependence. As the load increases, the winding operating temperature also increases due to the increase in winding loss, as shown in Fig. 7. This increase results in an increase in the shorted turn's resistance, which acts to reduce the circulating shorted turn current and thus the fault-induced heat.

The measurements in Fig. 11(b) illustrate that knowledge of the winding operating thermal status is key to understanding critical thermal conditions in fault presence. The fault-induced heat magnitude remains almost constant with load, as shown in Fig. 11(a). However, the winding temperature is considerably higher at high load and the thermal stress and resulting damaging effects of fault therefore expected to be more significant; the ITSCF neighboring healthy winding can be expected to thermally age faster at high load conditions and the fault to propagate relatively quicker.

2) Different Speed Conditions: To examine the fault thermal signature variation exclusive to operating speed change, the ITSCF cases examined in Section IV-C1 under FS are examined in this section under LS and HS and at constant load (C1, C4, and C7). For illustration, Fig. 12 shows the thermal measurements for ITSCF in coil5-C, while Fig. 12(a)
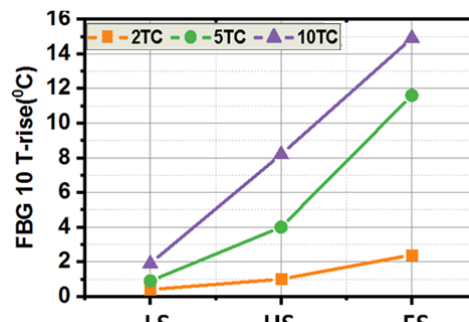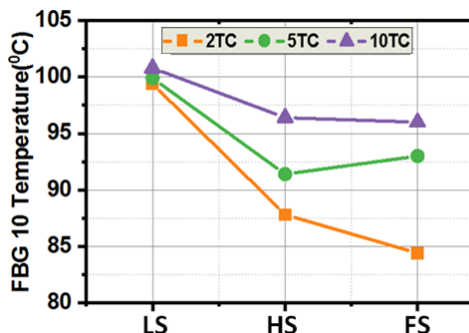
shows the corresponding measured temperature rise (healthy to faulty) and Fig. 12(b) shows the actual temperature measured by FBG10.

In contrast to the load variation impact on fault-induced thermal signature, the speed variation results in a considerable change in the fault-induced thermal signature. FBG10 recorded a temperature rise of ≈14.6 °C for the ten shorted turns case at FS (C1), which reduced to ≈8.2 °C and 2 °C at HS (C4) and LS (C7), respectively. The obtained thermal measurements illustrate that fault-induced heat detection is more challenging at lower speeds. The direct relationship between the operating speed and the fault induced thermal signature in the examined PMSM design is due to the shorted turn-induced EMF voltage speed dependence. Since the shorted turns essentially act as a shorted coil placed in the rotor magnetic field, the reduction in rotor speed causes a reduction in its back EMF and thus the circulating fault current, which in turn reduces the fault-induced heat. This was confirmed by the shorted turn-induced voltage and circulating currents measurements obtained during the tests. For illustration, Fig. 13 shows the measured shorted turn-induced current and voltage for the ten shorted turns case in coil5-C under FS, HS, and LS, demonstrating their clear reduction with the reduction in operating speed.

In the examined PMSM design, low-speed operation at full load generally reduces the cooling capability and thus results in winding operating temperature increase, as shown in Fig. 8. Therefore, despite the fault-induced temperature rise level largely reducing at lower speeds, the winding is still more thermally stressed in low-speed operation conditions, as shown in Fig. 12(b). This means that the time taken for the neighboring healthy turns insulation system degradation at low speed

(a) Measured shorted turns voltage
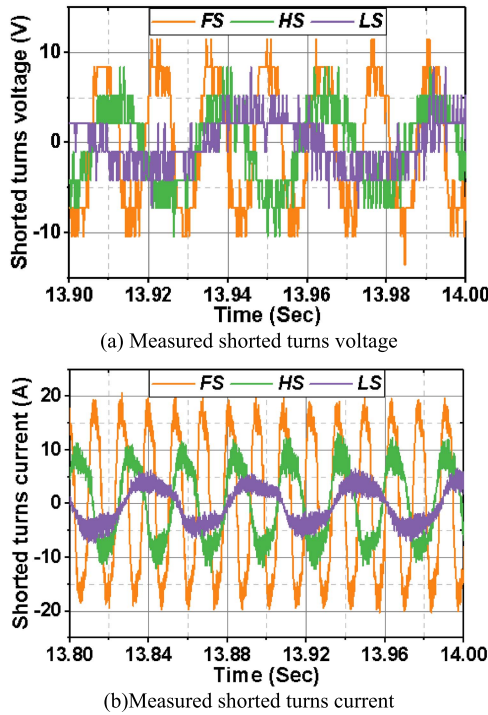

(b) Measured shorted turns current

Fig. 13. Measured shorted turn-induced voltage and current in coil5-C under different speed conditions. (a) Measured shorted turns voltage. (b) Measured shorted turns current.

(a) Measured T-rise by FBG10 at HL for the examined speeds

(b) Measured temperature by FBG10 at NL for the examined speed

Fig. 14. Fault-induced thermal signature behavior at different speeds/loads. (a) Measured T-rise by FBG10 at HL for the examined speeds. (b) Measured temperature by FBG10 at NL for the examined speed.

can generally be expected to be smaller than at high speed, and the fault can thus propagate relatively faster in low-speed conditions. However, it was discussed in Section IV-A2 and shown in Fig. 8 that the winding thermal characteristics of the test PMSM vary with different combinations of speed and load operating conditions. Further examination was therefore conducted to evaluate the critical thermal conditions in fault presence under LS, HS, and FS in HL and NL conditions (C2, C3, C5, C6, C8, and C9). Fig. 14 shows the obtained temperature measurements by FBG10 for a ten-turn ITSCF in coil5-C at HL [see Fig. 14(a)] and NL [see Fig. 14(b)]. The obtained thermal measurements show an opposite trend to that obtained at FL [see Fig. 12(b)]. For lower load conditions, the thermally critical operating point with fault is seen to be manifested at FS operation.

D. 2-D TSR Data Visualization

Effective interpretation of condition monitoring data is key in enabling its use for diagnostic decision making and maintenance management; this is particularly pertinent when performing diagnostics in critical systems with a large number of monitored components. Availability of a CM data advanced graphical interface could enable effective and straightforward interpretation of monitored diagnostic signals and any fault signatures contained and lead to improved reliability diagnosis. In addition, advanced CM data visualization could also enable easier simultaneous analysis of multiple components' health condition and ensure unambiguous CM data communication between diagnostic engineers. To this end, this section proposes the 2-D TSR thermal measurements' graphical form aimed at enabling straightforward and rapid interpretation of winding health conditions.
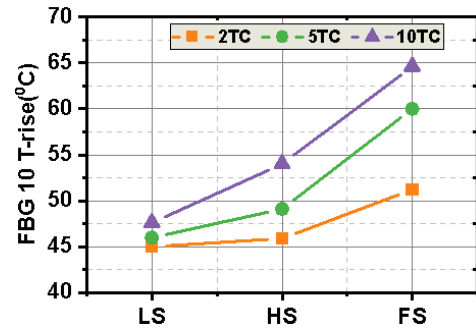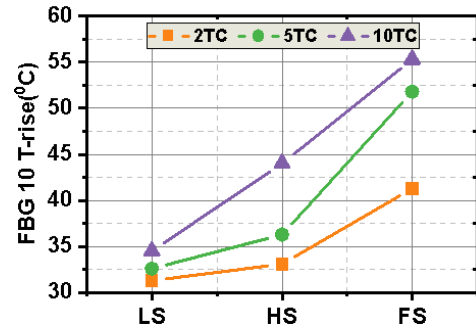
Fig. 15 shows a 2-D graphical representation of the examined PMSM end-winding radial thermal status measured by the 2-D TSR design. A contour heat-map graphical technique using OriginPro 2017 software was used to develop the 2-D end-winding graphical representation. The 12 dots shown in the 2-D graphical representation represent the FBG heads locations in the end winding, as shown in Fig. 4(b). The temperature gradient in the produced 2-D thermal image is automatically interpolated by the OriginPro software based on the updated FBGs thermal data. Fig. 15(a)–(c) shows the 2-D end-winding thermal representation when ITSCF was induced in the coil1-B for all examined fault severity at rated conditions (FS and FL). A hot spot can be clearly seen in the location of the fault [refer to fault locations in Fig. 4(c)], measured by FBG4 and FBG3. The hot spot temperature level increases with the shorted turns number increase to ≈91 °C for two-turn ITSCF, and ≈98 °C and ≈123 °C for five and ten ITSCF cases. In Fig. 15(e) and (f), the 2-D end-windings graphical model illustrates the end-winding thermal states when ITSCF was induced in coil2-A. The hot spot is displayed to the top of the 2-D model indicating both the fault presence and its location.

The presented visual aids could enable straightforward diagnosis of abnormal thermal conditions as well as their localization, with reduced requirements for diagnostic skills. Furthermore, the data visualization scheme could lead to development of advanced autonomous diagnostic systems, which link the 2-D thermal maps produced by *in situ* FBG sensors to automated on-line image processing algorithms in order to detect any abnormal changes in thermal conditions within the machine, and trend and locate these with a view to early diagnosis of any impending failure.
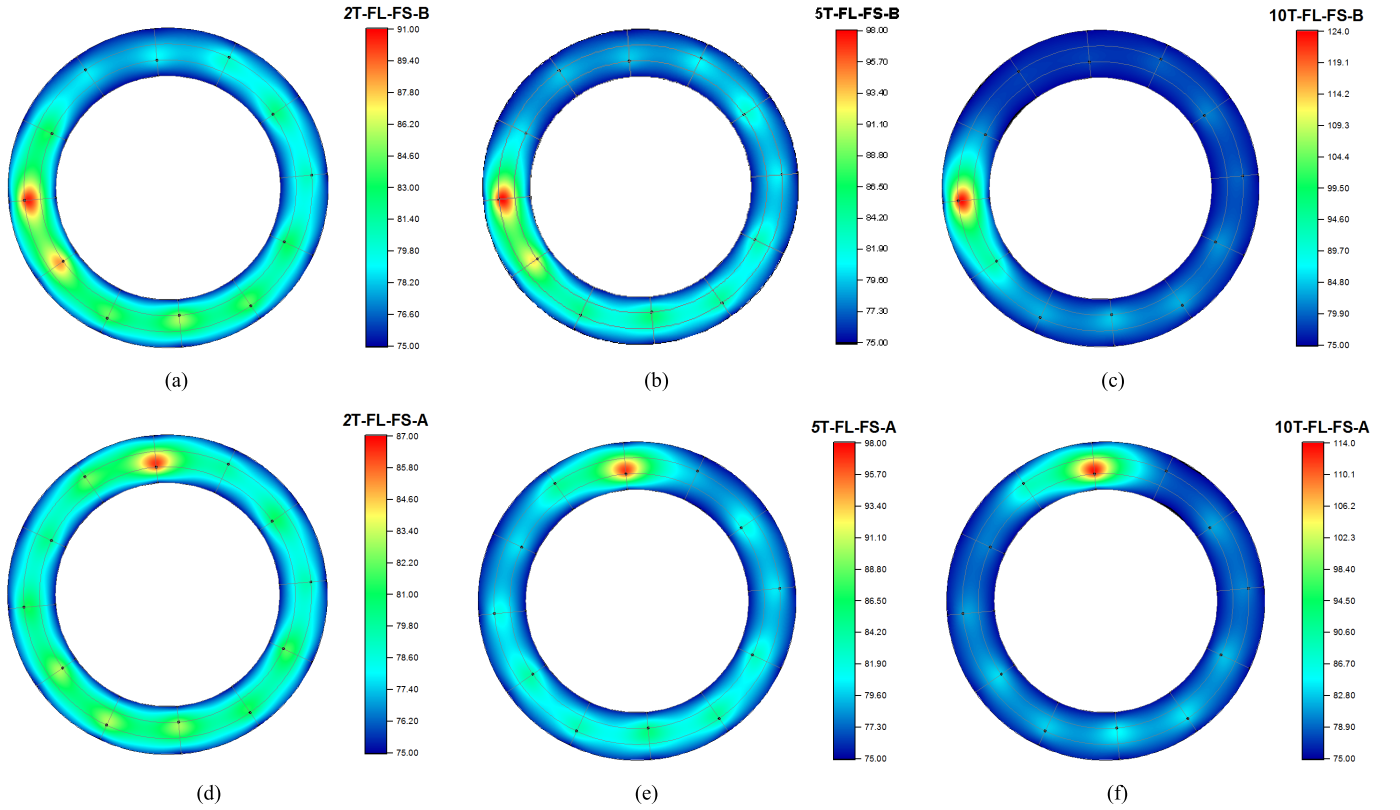
Fig. 15. End-winding thermal visualization using the 2-D representative model. (a) Two-turn, (b) five-turn, and (c) ten-turn ITSCF in phase B at FL and FS. (d) Two-turn, (e) five-turn, and (f) ten-turn ITSCF in phase A at FL and FS.

V. CONCLUSION

This article reported a new thermal sensing configuration for PM synchronous motors' stator winding on-line thermal and thus health condition diagnosis. The proposed sensing scheme is based on multiple thermal sensing points distributed within the stator end-winding section, practically achieved by designing a fiber optic 2-D TSR inscribed with a number of FBG heads. The following specific key conclusions arise from this article.

Fusing the unique PEEK packaging thermomechanical characteristics with FBG array multiplexing presents attractive opportunities for the improvement of current standard practices for end-winding thermal monitoring. The reported 2-D TSR was designed for and installed in a commercial inverter-driven PMSM's stator winding, and its performance examined in experiments under different healthy and faulty operating conditions. The proposed 2-D TSR design principles are, however, generalizable and applicable to a wide range of conventional end-winding topologies.

The results demonstrate the capability of the reported 2-D TSR design to effectively map the distributed thermal status of the PMSM winding in a wide range of healthy operating conditions.

The 2-D TSR is shown to enable unambiguous recognition of localized thermal excitation such as induced by ITSCFs and, thus, a clear diagnosis of ITSCFs in PMSMs, which remains a challenging task for conventional diagnostic techniques. This includes fault severity trending from low fault level but also the capability of fault location diagnosis.

The reported scheme enables improved understanding of ITSCF thermal signature manifestation in PMSMs. It is shown that load variation has no considerable impact on fault thermal signature, which is largely determined by operating speed. It was also shown that for the examined motor design, the critical operating point in ITSCF conditions is defined by both the operating speed and load; at high loads, the fault impact is higher at lower speed conditions (LS), while, in contrast, at low loads, the fault critical condition is manifested at FSs.

The reported 2-D TSR scheme enables inherent optimization of distributed sensing points and can facilitate more straightforward sensor installation when compared to the existing studies on FBG use for winding thermal monitoring.

Finally, this article reports the utilization of advanced graphical presentation of 2-D TSR distributed thermal measurement for improved understanding and usability of condition monitoring data and enhanced winding health diagnosis.

REFERENCES

[1] P. J. Tavner, "Review of condition monitoring of rotating electrical machines," *IET Electric Power Appl.*, vol. 2, no. 4, pp. 215–247, Jul. 2008.

[2] P. Zhang, Y. Du, T. G. Habetler, and B. Lu, "A survey of condition monitoring and protection methods for medium-voltage induction motors," *IEEE Trans. Ind. Appl.*, vol. 47, no. 1, pp. 34–46, Jan./Feb. 2011.

[3] T. D. Kefalas and A. G. Kladas, "Thermal investigation of permanent-magnet synchronous motor for aerospace applications," *IEEE Trans. Ind. Electron.*, vol. 61, no. 8, pp. 4404–4411, Aug. 2014.

[4] H. Jeong, S. Moon, and S. W. Kim, "An early stage interturn fault diagnosis of PMSMs by using negative-sequence components," *IEEE Trans. Ind. Electron.*, vol. 64, no. 7, pp. 5701–5708, Jul. 2017.

[5] A. G. Sarigiannidis, M. E. Beniakar, P. E. Kakosimos, A. G. Kladas, L. Papini, and C. Gerada, "Fault tolerant design of fractional slot winding permanent magnet aerospace actuator," *IEEE Trans. Transport. Electrific.*, vol. 2, no. 3, pp. 380–390, Sep. 2016.

[6] S. K. Kommuri, M. Defoort, H. R. Karimi, and K. C. Veluvolu, "A robust observer-based sensor fault-tolerant control for PMSM in electric vehicles," *IEEE Trans. Ind. Electron.*, vol. 63, no. 12, pp. 7671–7681, Dec. 2016.

[7] S. Choi *et al.*, "Fault diagnosis techniques for permanent magnet ac machine and drives—A review of current state of the art," *IEEE Trans. Transp. Electrific.*, vol. 4, no. 2, pp. 444–463, Jun. 2018.

[8] S. Grubic, J. M. Aller, B. Lu, and T. G. Habetler, "A survey on testing and monitoring methods for stator insulation systems of low-voltage induction machines focusing on turn insulation problems," *IEEE Trans. Ind. Electron.*, vol. 55, no. 12, pp. 4127–4136, Dec. 2008.

[9] W. Le Roux, R. G. Harley, and T. G. Habetler, "Detecting rotor faults in low power permanent magnet synchronous machines," *IEEE Trans. Power Electron.*, vol. 22, no. 1, pp. 322–328, Jan. 2007.

[10] M. A. Mazzoletti, G. R. Bossio, C. H. de Angelo, and D. R. Espinoza-Trejo, "A model-based strategy for interturn short-circuit fault diagnosis in PMSM," *IEEE Trans. Ind. Electron.*, vol. 64, no. 9, pp. 7218–7228, Sep. 2017.

[11] N. Leboeuf, T. Boileau, B. Nahid-Mobarakeh, N. Takorabet, F. Meibody-Tabar, and G. Clerc, "Estimating permanent-magnet motor parameters under inter-turn fault conditions," *IEEE Trans. Magn.*, vol. 48, no. 2, pp. 963–966, Feb. 2012.

[12] L. Romeral, J. C. Urresty, J.-R. R. Ruiz, and A. G. Espinosa, "Modeling of surface-mounted permanent magnet synchronous motors with stator winding interturn faults," *IEEE Trans. Ind. Electron.*, vol. 58, no. 5, pp. 1576–1585, May 2011.

[13] R. T. Meyer, R. A. DeCarlo, S. C. Johnson, and S. Pekarek, "Short-circuit fault detection observer design in a PMSM," *IEEE Trans. Aerosp. Electron. Syst.*, vol. 54, no. 6, pp. 3004–3017, Dec. 2018.

[14] R. M. Tallam *et al.*, "A survey of methods for detection of stator-related faults in induction machines," *IEEE Trans. Ind. Appl.*, vol. 43, no. 4, pp. 920–933, Jul./Aug. 2007.

[15] D. C. Patel and M. C. Chandorkar, "Modeling and analysis of stator interturn fault location effects on induction machines," *IEEE Trans. Ind. Electron.*, vol. 61, no. 9, pp. 4552–4564, Sep. 2014.

[16] S. D. Wilson, G. W. Jewell, and P. G. Stewart, "Resistance estimation for temperature determination in PMSMs through signal injection," in *Proc. IEEE Int. Conf. Electr. Mach. Drives*, San Antonio, TX, USA, May 2005, pp. 735–740.

[17] J. P. Bazzo, F. Mezzadri, E. V. da Silva, D. R. Pipa, C. Martelli, and J. C. C. da Silva, "Thermal imaging of hydroelectric generator stator using a DTS system," *IEEE Sensors J.*, vol. 15, no. 11, pp. 6689–6696, Nov. 2015.

[18] A. Mohammed and S. Djurović, "Stator winding internal thermal monitoring and analysis using *in Situ* FBG sensing technology," *IEEE Trans. Energy Convers.*, vol. 33, no. 3, pp. 1508–1518, Sep. 2018.

[19] A. Mohammed and S. Djurović, "FBG thermal sensing features for hot spot monitoring in random wound electric machine coils," *IEEE Sensors J.*, vol. 17, no. 10, pp. 3058–3067, May 2017.

[20] M. Fabian, D. M. Hind, C. Gerada, T. Sun, and T. V. K. Grattan, "Comprehensive monitoring of electrical machine parameters using an integrated fiber Bragg grating-based sensor system," *J. Lightw. Technol.*, vol. 36, no. 4, pp. 1046–1051, Feb. 2018.

[21] A. Mohammed, J. I. Melecio, and S. Djurović, "Stator winding fault thermal signature monitoring and analysis by *in Situ* FBG sensors," *IEEE Trans. Ind. Electron.*, vol. 66, no. 10, pp. 8082–8092, Oct. 2019.

[22] M. A. Valenzuela and G. Ramirez, "Thermal models for online detection of pulp obstructing the cooling system of TEFC induction motors in pulp area," in *IEEE Trans. Ind. Appl.*, vol. 47, no. 2, pp. 719–729, Mar./Apr. 2011.

[23] *Rotating Electrical Machines—Part 1: Rating and Performance*, Standard IEC 60034-1, 2010

[24] *IEEE Guide for AC Motor Protection, (Revision IEEE Std C37.96-2000)*, Standard IEEE Std C37.96-2012, Feb. 20, 2013, pp. 1–160.

Anees Mohammed received the M.Sc. degree in electrical power engineering from the University of Newcastle, Newcastle upon Tyne, U.K., in 2010, and the Ph.D. degree from The University of Manchester, Manchester, U.K., in 2019.

He is currently a Research Associate with the Department of Power Conversion, Electrical and Electronic Engineering, The University of Manchester. He spent four years as an Assistant Lecturer at Benghazi University, Benghazi, Libya. His current research interests include electric machines, drives, and condition monitoring.

Siniša Djurović (M'09) received the Dipl.Ing. degree in electrical engineering from the University of Montenegro, Podgorica, Montenegro, in 2002, and the Ph.D. degree from The University of Manchester, Manchester, U.K., in 2007.

He is currently a Senior Lecturer with the Power Conversion Group, The University of Manchester. His current research interests include the area of operation, design, monitoring, and diagnostics of electric machines and drives.